materials

MDPI

Article

Mott Insulator Ca_2RuO_4 under External Electric Field

Giuseppe Cuono and Carmine Autieri *

International Research Centre Magtop, Institute of Physics, Polish Academy of Sciences, Aleja Lotników 32/46, 02-668 Warsaw, Poland

* Correspondence: autieri@magtop.ifpan.edu.pl

Abstract: We have investigated the structural, electronic and magnetic properties of the Mott insulator Ca_2RuO_4 under the application of a static external electric field in two regimes: bulk systems at small fields and thin films at large electric fields. Ca_2RuO_4 presents S- and L-Pbca phases with short and long c lattice constants and with large and small band gaps, respectively. Using density functional perturbation theory, we have calculated the Born effective charges as response functions. Once we break the inversion symmetry by off-centering the Ru atoms, we calculate the piezoelectric properties of the system that suggest an elongation of the system under an electric field. Finally, we investigated a four-unit cell slab in larger electric fields, and we found insulator–metal transitions induced by the electric field. By looking at the local density of states, we have found that the gap gets closed on surface layers while the rest of the sample is insulating. Correlated to the electric-field-driven gap closure, there is an increase in the lattice constant c. Regarding the magnetic properties, we have identified two phase transitions in the magnetic moments with one surface that gets completely demagnetized at the largest field investigated. In all cases, the static electric field increases the lattice constant c and reduces the band gap of Ca_2RuO_4, playing a role in the competition between the L-phase and the S-phase.

Keywords: Mott insulator; transition metal oxides; electric field; born effective charges; density functional theory; piezoelectric tensor

Citation: Cuono, G.; Autieri, C. Mott Insulator Ca_2RuO_4 under External Electric Field. *Materials* **2022**, *15*, 6657. https://doi.org/10.3390/ma15196657

Academic Editors: Paolo Restuccia and James Ren

Received: 6 September 2022
Accepted: 23 September 2022
Published: 26 September 2022

1. Introduction

The study of compounds under the application of an external electric field has recently aroused great interest. One of the most important phenomena induced by the electric field is the control of the electronic properties of the systems. Among the several cases, great attention has recently been devoted to the manipulation of the insulator–metal Mott transition [1] via an external electric field. The control of the Mott transition can be useful for electronic devices, for example, as resistance RAM [2,3]. The application of the electric field is complementary to the application of pressure, with the important difference that pressure influences the electronic states by modifying the structural parameters, while the electric field directly controls the electronic states, with many technological advantages. A large electric field can control the carrier density in a region of an insulator; this is called electrostatic carrier doping [4,5].

Furthermore, an electric field can also break the inversion symmetry. As a consequence of the breaking of the inversion symmetry, in theoretical models, the hamiltonian is more anisotropic [6] and other terms in the hamiltonian are allowed as the spin-orbit Rashba [7,8] and the orbital Rahsba [9]. We have to mention that the breaking of the inversion symmetry can be introduced in many different ways, not only with an external electric field but also in the presence of surface, interfaces or inclusions [10,11]. In particular, the interface between ferroelectric and magnetic materials has been widely investigated in the last decade [12–14].

Ca_2RuO_4 (CRO) is a system that lends itself to analysis in the electrical field for its many phases and states [15–18] and where the scale associated with the Mott transition at T_{MI} = 357 K is much greater than that associated with antiferromagnetism at T_N = 110 K.

The magnetic and electronic properties of CRO are sensitive to the coupling of spin, charge and the orbital degrees of freedom [19,20]. It presents a Mott metal-insulator phase transition at T_{MI} = 357 K from a low-temperature Mott insulating phase to a high-temperature metallic phase [21]. This transition is accompanied by a structural transition, namely, the compound has a small *c*-axis in the low-temperature phase, called S-Pbca, and a longer *c* lattice constant in the high-temperature phase, named L-Pbca configuration; both S- and L-Pbca configurations are orthorombic. We know from the literature that the L-Pbca phase is metallic and the S-Pbca phase is insulating, and the lower energy orbital xy is full [22,23]. The unit cell contains four formula units with the RuO_6 octahedra settled in corner-shared planes alternated by CaO layers, as shown in Figure 1. It was shown that the Mott transition occurs because of the structural transition [22], and the occupation of the orbitals changes from a configuration with xz and yz occupied to one with xy occupied, bringing the system to an orbitally ordered state at low temperatures [24,25].

The Mott transition happens in the paramagnetic phase of the material at T_{MI}. However, it was found that insulator–metal transitions in CRO can be obtained under electric fields [26] or currents [27–29] at lower temperatures. Recently, a way to induce a pattern formation by means of an applied electric field in CRO has also been shown [30]. The electric field in this compound can modify the lattice constant c, producing a competition between structural phases with different c lattice constant. In this paper, we want to focus on the effect of the electric field on the experimental insulating S-Pbca phase and on the hypothetical insulating L-Pbca phase as benchmarks. The latter cannot be observed experimentally without an electric field, but the insulating L-Pbca could be stabilized by the electric field in future experiments.

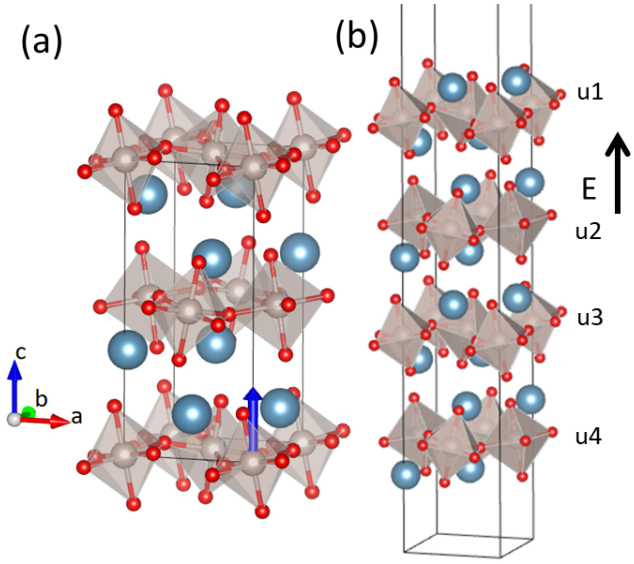

Figure 1. (**a**) Crystal structure of the CRO bulk. Grey, red and blue spheres indicate the Ru, O and Ca atoms, respectively. The blue arrow indicates the direction of the displacements of the Ru atoms when we break the inversion symmetry. (**b**) The four-unit cell slab. The black arrow indicates the direction of the applied electric field perpendicular to the surface. With u1, u2, u3 and u4 we indicate the four-unit cells.

Paper Organization

In this paper, we study the structural, electronic and magnetic properties of Ca_2RuO_4 under the application of an external electric field with a theoretical, computational analysis by using the ab initio density functional theory (DFT) method. We analyze both the regions of small and large applied electric fields. In the first region, we focus on the bulk, and we calculate the response functions, while in the second one, we build a four-unit cell slab, and we investigate the local density of the states, equilibrium *c*-axis, band gap and magnetic moments of the Ru atoms. The paper is organized as follows: in the next section, we report

the computational details, while in the third section, we present our results. Finally, in the last section, we draw our conclusions.

2. Computational Details

Our DFT simulations have been performed by employing the Vienna ab initio simulation package (VASP) [31–33]. The projector augmented wave (PAW) [34] technique has been used for the core and the valence electrons, with a cutoff of 480 eV for the plane-wave basis. The calculations have been performed with an $11 \times 11 \times 4$ k-points grid for the bulk and a $14 \times 14 \times 1$ k-points grid for the slab, all centered in Γ. The Local Density Approximation is enough to describe the metallic phases of ruthenates. For the treatment of exchange correlation, the Perdew–Burke–Ernzerhof (PBE) [35] generalized gradient approximation (GGA) has been used, and we have also considered the correlations for the Ru-4*d* states by using a Coulomb repulsion U = 3 eV on the Ru atoms in the antiferromagnetic insulating state [36]. For the Hund coupling, we have used a value in agreement with the literature for the $4d/5d$ electrons [37], namely, J_H = 0.15 U has been employed. The experimental lattice constants are a_{short} = 5.3945 Å, b_{short} = 5.5999 Å, c_{short} = 11.7653 Å in the S-Pbca phase and a_{long} = 5.3606 Å, b_{long} = 5.3507 Å, c_{long} = 12.2637 Å in the L-Pbca phase [38]. For the calculation of the Born effective charges Z^* and the piezoelectric tensor in the bulk, we have used the modern theory of polarization [39,40] and the self-consistent response to finite electric fields [41,42] for bulk systems as implemented in VASP. For the thin film, we have constructed four-unit cells along the (001) direction, and we have added the electric field in the direction (001) perpendicular to thin film surfaces performing the same strategy used for several 2D materials in the electric field [43,44]. In the case of the slab, we have considered the dipole corrections to the potential as implemented in VASP in order to avoid interactions between the periodically repeated images [45]. Density functional theory does not fully reproduce the properties of the Mott insulator at high temperatures. Therefore, deviations from the DFT results are expected once we would include many-body and dynamical effects in the self-energy, which is a relevant property of many-body systems, especially in the non-magnetic phase and close to the Mott transition at T_{MI}.

3. Results

We divide our results into three subsections. In the first subsection, we report the investigation of the bulk with inversion symmetry. In the second one, we calculate the piezoelectric tensor after breaking the inversion symmetry by shifting the positions of the Ru atoms along the *z*-axis. The direction of the displacements of the Ru is shown in Figure 1a. In the third subsection, we analyze the properties of a four-unit cell slab, shown in Figure 1b, without and with the application of an external electric field.

3.1. Properties of the Bulk with Inversion Symmetry

In this subsection, we analyze the Ca_2RuO_4 bulk without and with the application of an external electric field. First, we have compressed and elongated the system along the *c*-axis both in the S- and L-Pbca phases and we have investigated how the energy of the compound varies as a function of the lattice constant c. We have taken into consideration both the non-magnetic and the magnetic cases. In Figure 2, we report the energy of the S- and L-Pbca phases as a function of the *c*-axis in panel (a) in the non-magnetic phase while in panel (b) in the magnetic phase. In the latter case, the Ru atoms of the primitive cell are in the checkerboard antiferromagnetic configuration. In both cases, the L-Pbca phase has a theoretical value of the c lattice constant larger than the S-phase. The difference between the theoretical and experimental c lattice constants is of the order of 1% for the non-magnetic phases and Of the order of 2% for the magnetic phases. The non-magnetic phases are metallic, while the antiferromagnetic phases are insulating. Even without considering THE dynamical effects, we obtained that in the metallic phase, the L-Pbca phase is the ground state, while in the insulating phase, the S-phase is the ground state in agreement with the

experimental results. In the bulk, the band gaps of the antiferromagnetic phases are 0.88 and 0.72 eV for the S- and L-Pbca phases, respectively.

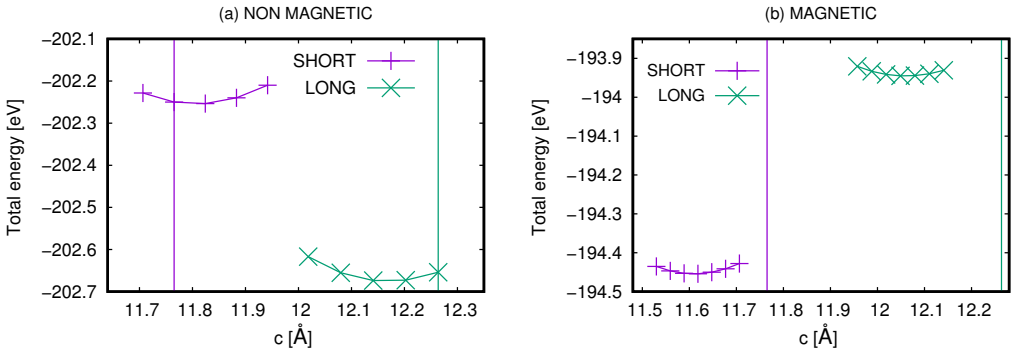

Figure 2. Total energy of the system as a function of the lattice constant c in the (**a**) non-magnetic and (**b**) in the magnetic case for the L- and S-Pbca phaseS. The in-plane lattice parameters have been fixed to the experimental values [38] reported in the computational details.

Then, we applied an electric field along the z-direction for the S-Pbca phase, with qE = 5×10^{-4} eV/Å = 5×10^{4} eV/cm, where E is the electric field, and q is the elementary charge, and we calculated the response functions of the system, such as the Born effective charges Z^*. For larger electric fields, the numerical simulations do not converge because we are close to the onset of Zener tunneling [42]. Under electric fields of this order of magnitude, the system is an insulator, and the gap is 0.60 eV for the short crystal structure. Therefore, even a relatively small electric field tends to close the band gap and could favor the formation of the L-phase that has a smaller gap. Within the density functional perturbation theory, Z^* are defined as [46]:

$$Z_{ij}^{*A} = \frac{1}{q}\frac{\partial F_i^A}{\partial E_j}, \tag{1}$$

with $i, j = x, y, z$, and where E_j is the electric field applied along the j-direction while F_i^A is the force that acts on the ion in the i-direction on atom A.

The Z^* are reported in Table 1. As expected, diagonal Z^* are positive for the cation Ca and Ru, while they are negative for the oxygen anions. We have obtained large Z^*, especially for the cation Ca. Similarly, large Z^* were also observed in other transition-metal oxides [47]. The largest Z^* diagonal element for the Ru atoms is given by Z^*_{zz} = 1.193 $|e|$, which indicates that under an electric field along the z-direction, a component of the force acting on the Ru atoms is along the z-axis. The diagonal terms are the largest for both Ca and O atoms but not for the Ru. Indeed, we have found large off-diagonal terms for the Ru atoms up to Z^*_{yz} = 3.121 $|e|$, which is much larger than Z^*_{zz}. Therefore, under an electric field in the z-direction, there is also a component of the force on the Ru atoms acting along the y-axis. Large Z^* off-diagonal terms were already observed for highly distorted transition metals perovskites [48], even if we did not find cases where off-diagonal Z^* terms are larger than diagonal Z^* terms as they appear for the Ru in the literature. Due to the symmetry of the system, the Z^*_{ij} tensor is not diagonalizable, as we can see for the Ru case with spin up: $Z_{ij}^{*Ru_\uparrow} = \begin{pmatrix} 0.045 & -0.464 & -0.119 \\ 0.412 & 0.037 & 3.121 \\ 0.409 & 0.377 & 1.193 \end{pmatrix}$. A diagonal Z^*_{ij} tensor in perovskites can be obtained in the absence of octahedral tilts and distortions, however, the undistorted Ca_2RuO_4 would be metallic as for the Sr_2RuO_4.

Table 1. Z^* tensors for the bulk in the S-phase. O_1 and O_2 are the basal and the apical oxygens, respectively. $Ru_\uparrow$ and $Ru_\downarrow$ are the two Ru with opposite magnetic moments since we are considering the checkerboard antiferromagnetic configuration.

Ion	Z^*_{xx}	Z^*_{xy}	Z^*_{xz}	Z^*_{yx}	Z^*_{yy}	Z^*_{yz}	Z^*_{zx}	Z^*_{zy}	Z^*_{zz}
Ca	9.331	−0.089	0.087	−0.138	9.288	−2.594	0.172	0.088	8.875
O_1	−4.794	−1.101	0.128	−1.003	−4.656	−1.471	0.129	0.054	−3.558
O_2	−4.558	−0.017	0.383	−0.299	−4.651	−1.355	0.227	0.126	−5.915
$Ru_\uparrow$	0.045	−0.464	−0.119	0.412	0.037	3.121	−0.409	0.377	1.193
$Ru_\downarrow$	0.045	0.464	0.119	−0.412	0.037	3.121	0.409	0.377	1.193

3.2. Properties of the Bulk without Inversion Symmetry

We also calculate the piezoelectric tensor, which is zero for centrosymmetric crystal structures [49]. Therefore, in order to obtain a piezoelectric tensor different from zero in systems such as Ca_2RuO_4 we have to break the inversion symmetry [50–52]. We have shifted the Ru atoms along the *z*-axis to break the inversion symmetry, as shown in Figure 1a, and we have calculated the components of the tensor. The Ru atoms have been moved by 0.023, 0.046 and 0.069 Å along the positive direction of the *z*-axis, and we studied how the piezoelectric components vary at different values of the positions of the Ru atoms for both clamped and relaxed contributions. The piezoelectric tensor is defined as [53]:

$$\epsilon^0_{ij} = -\frac{\partial \sigma_i}{\partial E_j}, \tag{2}$$

where $i = xx, yy, zz, xy, yz, zx$ and $j = x, y, z$. We can also use the notation i = 1, 2, 3, 4, 5, 6 and j = 1, 2, 3.

The results are reported in Figure 3. We report both the ion-clamped (panels a and b) and the relaxed contributions (panels c and d), where the latter ones are the contributions that include ionic relaxation. With diagonal and off-diagonal we refer to the components of the stress tensor, namely, the diagonal components are $i = xx, yy, zz$ (i = 1, 2, 3), while off-diagonal are those with $i = xy, yz, zx$ (i = 4, 5, 6). We can see from the figure that, both in the cases of ion-clamped and relaxed contributions, the diagonal terms are one order of magnitude greater than the off-diagonal elements. The diagonal terms are zero in the case of centrosymmetric crystal structure, while they become different from zero when we break the inversion symmetry, and they are almost constant at different values of the displacement of the Ru atoms, while the off-diagonal terms show a linear behavior in the case of ion-clamped contributions while a more complex trend in the case of the relaxed contributions. From these results, we can state that in the case of breaking of the inversion symmetry due, for example, to the presence of interfaces or electric fields, the compound can show piezoelectric features. The positive value of the diagonal components means that the system would increase its volume under an external static electric field.

3.3. Properties of the Slab at Large Electric Fields

We have analyzed a four-unit cell slab with a vacuum of 20 Å, as shown in Figure 1b, for both the S- and L-Pbca phases. We have compressed and elongated the lattice constant c and we have studied the slab without and with the application of an external electric field. In the absence of the electric field, the results show a shift of the equilibrium *c*-axis to lower values with respect to the bulk for both the L- and S-Pbca phases. Then, we studied the slab under the application of an external electric field. In Figure 4, the gap at a fixed value of the *c*-axis, namely, c_{short}, and the equilibrium *c*-axis for the S-Pbca phase, as a function of the electric field, are reported. We can see that great values of the electric field close the gap and bring the system to a metallic state. The gap gets closed

at qE = 0.06 eV/Å = 6×10^6 eV/cm, and a new gap appears twice; then, the electric field definitively closes the gap at 0.11 eV/Å.

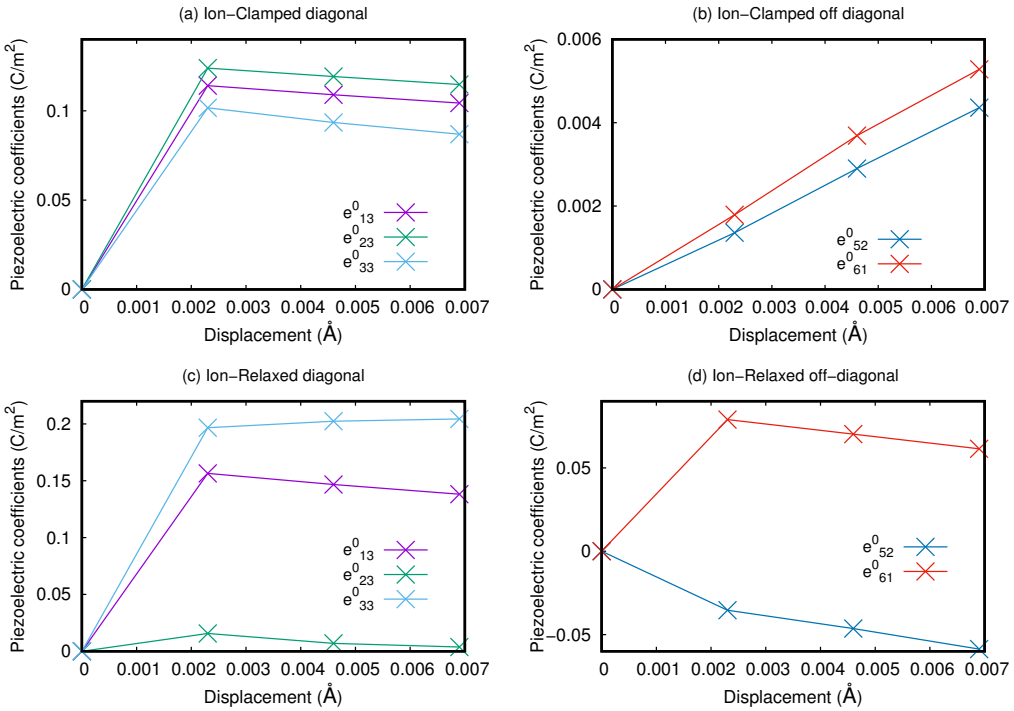

Figure 3. Evolution of the piezoelectric components for the S-phase as a function of the displacement of the Ru atoms along the *z*-axis for the bulk. We report the ion-clamped and ion-relaxed cases (diagonal and off-diagonal refer to the components of the stress tensor) in panels (**a**–**d**).

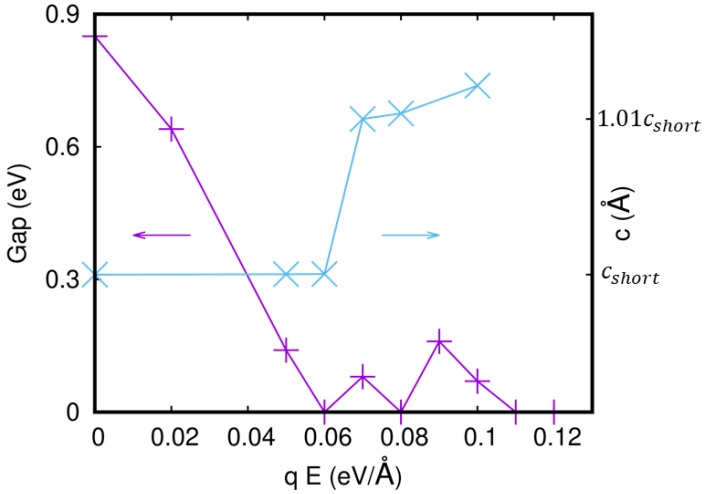

Figure 4. Gap and equilibrium *c*-axis as a function of the electric field in the slab for the S-Pbca phase.

There is a phase transition in the equilibrium *c*-axis when the gap gets closed at qE = 0.06 eV/Å. We have used a parabolic fit of the values of the equilibrium *c*-axis as a function of the applied electric field, and we have found that the values of c always increase as the values of the applied field increase. We also report the local density of states projected on the *d*-orbitals of the Ru atoms of the four surfaces. We show the DOS at two fields, qE = 0 and qE = 0.06 eV/Å, in Figures 5 and 6, respectively. In the first case, the system is insulating, and in the second, it is metallic. By looking at the local density of the states, we can state that the electric field at qE = 0.06 eV/Å closes the gap on the

surfaces while the rest of the sample is insulating. The system has metallic layers in the same fashion as the two-dimensional electron gas.

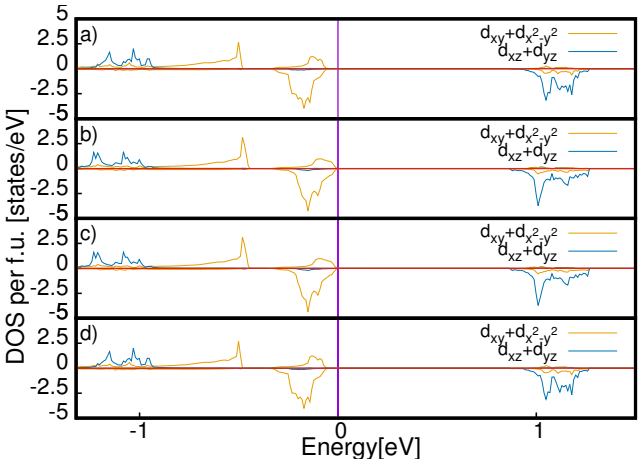

Figure 5. Local density of states (LDOS) for the *d*-orbitals of the Ru atoms of the four layers at E = 0 eV for the S-Pbca phase in a range between −5 and 5 eV. The LDOS related to d_{xz} and d_{yz} orbitals is divided by 3 for better visualization. We report the LDOS for the unit cells u1, u2, u3 and u4 in panels (**a**), (**b**) (**c**) and (**d**), respectively.

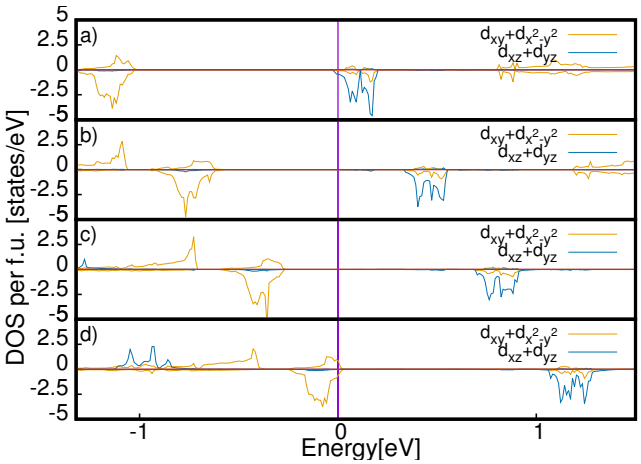

Figure 6. Local density of states for the *d*-orbitals of the Ru atoms of the four layers at qE = 0.06 eV/Å for the S-Pbca phase in a range between −5 and 5 eV. The LDOS related to d_{xz} and d_{yz} orbitals is divided by 3 for a better visualization.. We report the LDOS for the unit cells u1, u2, u3 and u4 in panels (**a**), (**b**) (**c**) and (**d**), respectively.

In Figure 7, the gap and the magnetic moments of the Ru atoms of the two surfaces at a fixed value of the *c*-axis (c_{short}) for the S-Pbca phase are reported. We can identify two phase transitions in the magnetic moments. The magnetic moments of the two surfaces have opposite behavior starting from the point where the gap is closed the first time, namely, at qE = 0.06 eV/Å, one magnetic moment decreases and another increases its value. Then, starting from qE = 0.08 eV/Å both magnetic moments decrease, but only one Ru surface gets demagnetized. For the L-Pbca phase, we get very similar results, but the closing of the gap is shifted to lower values of the electric field because the gap is smaller in the L-Pbca phase. The magnetic moments of the Ru and the gap for the L-Pbca phase as a function of the electric field at a fixed value of the *c*-axis (c_{long}) are reported in Figure 8.

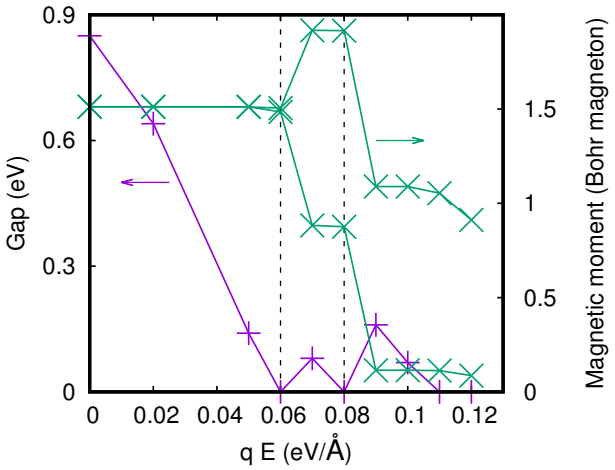

Figure 7. Gap and magnetic moments of the Ru atoms of the two surfaces as a function of the electric field in the slab for the S-Pbca phase.

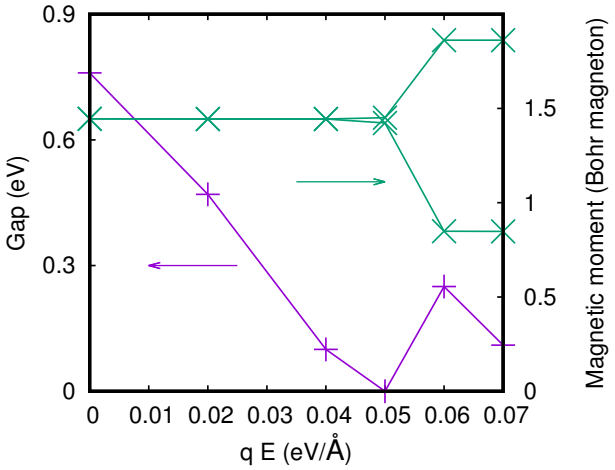

Figure 8. Gap and magnetic moments of the Ru atoms of the two surfaces as a function of the electric field in the slab for the L-Pbca phase.

The competition between these different metallic and insulating phases in CRO starts from electric fields around 0.06 eV/Å in the S-phase. At the electric fields studied in bulk, we are very far from the insulating-metal transition. As a consequence of the volume changes under the electric field, there will also be changes in the octahedral rotations [54] that we do not analyze here.

4. Conclusions

We have studied the structural, electronic and magnetic properties of Ca_2RuO_4 under the application of an external electric field using first-principles calculations. We have analyzed the bulk at low electric fields and a slab of four-unit cells at large fields. In the region of small electric fields, we have studied the Ca_2RuO_4 bulk and we have found that the system is insulating. We have calculated the Born effective charges and the piezoelectric tensor. To simulate the presence of interfaces and surfaces, we have broken the inversion symmetry by off-centering the Ru atom to obtain the piezoelectric tensor different from zero. The positive value of the diagonal elements of the piezoelectric tensor reveals that the system tends to elongate under the applied electric field.

Finally, we have studied a four-unit cell slab up to large electric fields, and we have found an insulator–metal transition occurring in the system at large electric fields. If we look at the density of states when the gap is closed, we can see that this happens in two of the four-unit cells considered. Therefore, we are in a two-dimensional electron gas phase.

The competition between these different metallic and insulating phases in CRO starts from electric fields around 0.06 eV/Å in the S-phase. Regarding the magnetic properties, we have found two phase transitions in the magnetic moments. For the L-Pbca phase, we get very similar results ,but the closing of the gap is shifted to lower values of the electric field. Even considering the modeling limitations due to the absence of many-body and dynamical effects, in all simulated cases, the static electric field increases the lattice constant c and reduces the band gap of Ca_2RuO_4. This plays a role in the competition between the L-Pbca phase and the S-Pbca phase, especially close to the transition temperature T_{MI}.

Author Contributions: Conceptualization, C.A.; Data curation, G.C.; Investigation, G.C.; Methodology, G.C.; Writing—original draft, G.C.; Writing—review & editing, C.A. All authors have read and agreed to the published version of the manuscript

Funding: The work is supported by the Foundation for Polish Science through the International Research Agendas program co-financed by the European Union within the Smart Growth Operational Programme.

Institutional Review Board Statement: Not applicable.

Informed Consent Statement: Not applicable.

Data Availability Statement: The data that support the findings of this study are available on request from the corresponding author.

Acknowledgments: We thank M. Cuoco, C. Noce and F. Forte for useful discussions. We acknowledge the access to the computing facilities of the Interdisciplinary Center of Modeling at the University of Warsaw, Grants G75-10, G84-0 and GB84-1. We acknowledge the CINECA award under the ISCRA initiatives IsC93 "RATIO" and IsC99 "SILENTS" grant, for the availability of high-performance computing resources and support.

Conflicts of Interest: The authors declare no conflict of interest.

References

1. Imada, M.; Fujimori, A.; Tokura, Y. Metal-insulator transitions. *Rev. Mod. Phys.* **1998**, *70*, 1039–1263. [CrossRef]
2. Meijer, G.I. Who wins the nonvolatile memory race? *Science* **2008**, *319*, 1625–1626. [CrossRef] [PubMed]
3. Waser, R.; Aono, M. Nanoionics-based resistive switching memories. *Nat. Mater.* **2007**, *6*, 833–840. [CrossRef]
4. Rozenberg, M.J.; Inoue, I.H.; Sánchez, M.J. Nonvolatile Memory with Multilevel Switching: A Basic Model. *Phys. Rev. Lett.* **2004**, *92*, 178302. [CrossRef]
5. Inoue, I.H.; Rozenberg, M.J. Taming the Mott Transition for a Novel Mott Transistor. *Adv. Funct. Mater.* **2008**, *18*, 2289–2292. [CrossRef]
6. van Thiel, T.C.; Fowlie, J.; Autieri, C.; Manca, N.; Šiškins, M.; Afanasiev, D.; Gariglio, S.; Caviglia, A.D. Coupling Lattice Instabilities across the Interface in Ultrathin Oxide Heterostructures. *ACS Mater. Lett.* **2020**, *2*, 389–394. [CrossRef] [PubMed]
7. Autieri, C.; Barone, P.; Sławińska, J.; Picozzi, S. Persistent spin helix in Rashba-Dresselhaus ferroelectric $CsBiNb_2O_7$. *Phys. Rev. Mater.* **2019**, *3*, 084416. [CrossRef]
8. Hussain, G.; Samad, A.; Rehman, M.U.; Cuono, G.; Autieri, C. Emergence of Rashba splitting and spin-valley properties in Janus $MoGeSiP_2As_2$ and $WGeSiP_2As_2$ monolayers. *J. Magn. Magn. Mater.* **2022**, *563*, 169897. [CrossRef]
9. van Thiel, T.C.; Brzezicki, W.; Autieri, C.; Hortensius, J.R.; Afanasiev, D.; Gauquelin, N.; Jannis, D.; Janssen, N.; Groenendijk, D.J.; Fatermans, J.; et al. Coupling Charge and Topological Reconstructions at Polar Oxide Interfaces. *Phys. Rev. Lett.* **2021**, *127*, 127202. [CrossRef] [PubMed]
10. Autieri, C.; Cuoco, M.; Noce, C. Structural and electronic properties of $Sr_2RuO_4/Sr_3Ru_2O_7$ heterostructures. *Phys. Rev. B* **2014**, *89*, 075102. [CrossRef]
11. Autieri, C.; Cuoco, M.; Noce, C. Collective properties of eutectic ruthenates: Role of nanometric inclusions. *Phys. Rev. B* **2012**, *85*, 075126. [CrossRef]
12. Paul, A.; Reitinger, C.; Autieri, C.; Sanyal, B.; Kreuzpaintner, W.; Jutimoosik, J.; Yimnirun, R.; Bern, F.; Esquinazi, P.; Korelis, P.; et al. Exotic exchange bias at epitaxial ferroelectric-ferromagnetic interfaces. *Appl. Phys. Lett.* **2014**, *105*, 022409. [CrossRef]
13. Autieri, C.; Sanyal, B. Unusual ferromagnetic $YMnO_3$ phase in $YMnO_3/La_{2/3}Sr_{1/3}MnO_3$ heterostructures. *New J. Phys.* **2014**, *16*, 113031. [CrossRef]
14. Hausmann, S.; Ye, J.; Aoki, T.; Zheng, J.G.; Stahn, J.; Bern, F.; Chen, B.; Autieri, C.; Sanyal, B.; Esquinazi, P.D.; et al. Atomic-scale engineering of ferroelectric-ferromagnetic interfaces of epitaxial perovskite films for functional properties. *Sci. Rep.* **2017**, *7*, 10734. [CrossRef]

15. Nakatsuji, S.; Maeno, Y. Quasi-Two-Dimensional Mott Transition System $Ca_{2-x}Sr_xRuO_4$. *Phys. Rev. Lett.* **2000**, *84*, 2666–2669. [CrossRef] [PubMed]
16. Cuoco, M.; Forte, F.; Noce, C. Interplay of Coulomb interactions and *c*-axis octahedra distortions in single-layer ruthenates. *Phys. Rev. B* **2006**, *74*, 195124. [CrossRef]
17. Forte, F.; Cuoco, M.; Noce, C. Field-induced orbital patterns in ferromagnetic layered ruthenates. *Phys. Rev. B* **2010**, *82*, 155104. [CrossRef]
18. Pincini, D.; Veiga, L.S.I.; Dashwood, C.D.; Forte, F.; Cuoco, M.; Perry, R.S.; Bencok, P.; Boothroyd, A.T.; McMorrow, D.F. Tuning of the Ru^{4+} ground-state orbital population in the $4d^4$ Mott insulator Ca_2RuO_4 achieved by La doping. *Phys. Rev. B* **2019**, *99*, 075125. [CrossRef]
19. Koga, A.; Kawakami, N.; Rice, T.M.; Sigrist, M. Orbital-Selective Mott Transitions in the Degenerate Hubbard Model. *Phys. Rev. Lett.* **2004**, *92*, 216402. [CrossRef]
20. Das, L.; Forte, F.; Fittipaldi, R.; Fatuzzo, C.G.; Granata, V.; Ivashko, O.; Horio, M.; Schindler, F.; Dantz, M.; Tseng, Y.; et al. Spin-Orbital Excitations in Ca_2RuO_4 Revealed by Resonant Inelastic X-Ray Scattering. *Phys. Rev. X* **2018**, *8*, 011048. [CrossRef]
21. Alexander, C.S.; Cao, G.; Dobrosavljevic, V.; McCall, S.; Crow, J.E.; Lochner, E.; Guertin, R.P. Destruction of the Mott insulating ground state of Ca_2RuO_4 by a structural transition. *Phys. Rev. B* **1999**, *60*, R8422–R8425. [CrossRef]
22. Gorelov, E.; Karolak, M.; Wehling, T.O.; Lechermann, F.; Lichtenstein, A.I.; Pavarini, E. Nature of the Mott Transition in Ca_2RuO_4. *Phys. Rev. Lett.* **2010**, *104*, 226401. [CrossRef]
23. Zhang, G.; Pavarini, E. Mott transition, spin-orbit effects, and magnetism in Ca_2RuO_4. *Phys. Rev. B* **2017**, *95*, 075145. [CrossRef]
24. Okazaki, R.; Nishina, Y.; Yasui, Y.; Nakamura, F.; Suzuki, T.; Terasaki, I. Current-Induced Gap Suppression in the Mott Insulator Ca_2RuO_4. *J. Phys. Soc. Jpn.* **2013**, *82*, 103702. [CrossRef]
25. Porter, D.G.; Granata, V.; Forte, F.; Di Matteo, S.; Cuoco, M.; Fittipaldi, R.; Vecchione, A.; Bombardi, A. Magnetic anisotropy and orbital ordering in Ca_2RuO_4. *Phys. Rev. B* **2018**, *98*, 125142. [CrossRef]
26. Nakamura, F.; Sakaki, M.; Yamanaka, Y.; Tamaru, S.; Suzuki, T.; Maeno, Y. Electric-field-induced metal maintained by current of the Mott insulator Ca_2RuO_4. *Sci. Rep.* **2013**, *3*, 2536. [CrossRef]
27. Zhang, J.; McLeod, A.S.; Han, Q.; Chen, X.; Bechtel, H.A.; Yao, Z.; Gilbert Corder, S.N.; Ciavatti, T.; Tao, T.H.; Aronson, M.; et al. Nano-Resolved Current-Induced Insulator-Metal Transition in the Mott Insulator Ca_2RuO_4. *Phys. Rev. X* **2019**, *9*, 011032. [CrossRef]
28. Cirillo, C.; Granata, V.; Avallone, G.; Fittipaldi, R.; Attanasio, C.; Avella, A.; Vecchione, A. Emergence of a metallic metastable phase induced by electrical current in Ca_2RuO_4. *Phys. Rev. B* **2019**, *100*, 235142. [CrossRef]
29. Mattoni, G.; Yonezawa, S.; Nakamura, F.; Maeno, Y. Role of local temperature in the current-driven metal–insulator transition of Ca_2RuO_4. *Phys. Rev. Mater.* **2020**, *4*, 114414. [CrossRef]
30. Gauquelin, N.; Forte, F.; Jannis, D.; Fittipaldi, R.; Autieri, C.; Cuono, G.; Granata, V.; Lettieri, M.; Noce, C.; Miletto Granozio, F.; et al. Pattern Formation by Electric-field Quench in Mott Crystal. *Submitted*.
31. Kresse, G.; Hafner, J. Ab initio molecular dynamics for liquid metals. *Phys. Rev. B* **1993**, *47*, 558–561. [CrossRef]
32. Kresse, G.; Furthmüller, J. Efficiency of ab-initio total energy calculations for metals and semiconductors using a plane-wave basis set. *Comput. Mater. Sci.* **1996**, *6*, 15–50. [CrossRef]
33. Kresse, G.; Furthmüller, J. Efficient iterative schemes for ab initio total-energy calculations using a plane-wave basis set. *Phys. Rev. B* **1996**, *54*, 11169. [CrossRef]
34. Kresse, G.; Joubert, D. From ultrasoft pseudopotentials to the projector augmented-wave method. *Phys. Rev. B* **1999**, *59*, 1758–1775. [CrossRef]
35. Perdew, J.P.; Ruzsinszky, A.; Csonka, G.I.; Vydrov, O.A.; Scuseria, G.E.; Constantin, L.A.; Zhou, X.; Burke, K. Restoring the Density-Gradient Expansion for Exchange in Solids and Surfaces. *Phys. Rev. Lett.* **2008**, *100*, 136406. [CrossRef]
36. Autieri, C. Antiferromagnetic *xy* ferro-orbital order in insulating $SrRuO_3$ thin films with SrO termination. *J. Phys. Condens. Matter* **2016**, *28*, 426004. [CrossRef]
37. Vaugier, L.; Jiang, H.; Biermann, S. Hubbard *U* and Hund exchange *J* in transition metal oxides: Screening versus localization trends from constrained random phase approximation. *Phys. Rev. B* **2012**, *86*, 165105. [CrossRef]
38. Friedt, O.; Braden, M.; André, G.; Adelmann, P.; Nakatsuji, S.; Maeno, Y. Structural and magnetic aspects of the metal-insulator transition in $Ca_{2-x}Sr_xRuO_4$. *Phys. Rev. B* **2001**, *63*, 174432. [CrossRef]
39. Resta, R. Theory of the electric polarization in crystals. *Ferroelectrics* **1992**, *136*, 51–55. [CrossRef]
40. King-Smith, R.D.; Vanderbilt, D. Theory of polarization of crystalline solids. *Phys. Rev. B* **1993**, *47*, 1651–1654. [CrossRef]
41. Nunes, R.W.; Gonze, X. Berry-phase treatment of the homogeneous electric field perturbation in insulators. *Phys. Rev. B* **2001**, *63*, 155107. [CrossRef]
42. Souza, I.; Íñiguez, J.; Vanderbilt, D. First-Principles Approach to Insulators in Finite Electric Fields. *Phys. Rev. Lett.* **2002**, *89*, 117602. [CrossRef]
43. Islam, R.; Ghosh, B.; Autieri, C.; Chowdhury, S.; Bansil, A.; Agarwal, A.; Singh, B. Tunable spin polarization and electronic structure of bottom-up synthesized $MoSi_2N_4$ materials. *Phys. Rev. B* **2021**, *104*, L201112. [CrossRef]
44. Islam, R.; Verma, R.; Ghosh, B.; Muhammad, Z.; Bansil, A.; Autieri, C.; Singh, B. Switchable Large-Gap Quantum Spin Hall State in Two-Dimensional MSi_2Z_4 Materials Class. *arXiv* **2022**, arXiv:2207.08407. [CrossRef]

45. Neugebauer, J.; Scheffler, M. Adsorbate-substrate and adsorbate-adsorbate interactions of Na and K adlayers on Al(111). *Phys. Rev. B* **1992**, *46*, 16067–16080. [CrossRef]
46. Gonze, X.; Lee, C. Dynamical matrices, Born effective charges, dielectric permittivity tensors, and interatomic force constants from density-functional perturbation theory. *Phys. Rev. B* **1997**, *55*, 10355–10368. [CrossRef]
47. Detraux, F.; Ghosez, P.; Gonze, X. Anomalously large Born effective charges in cubic WO_3. *Phys. Rev. B* **1997**, *56*, 983–985. [CrossRef]
48. Ganga Prasad, K.; Niranjan, M.K.; Asthana, S.; Karthikeyan, R. Investigation of Raman Modes and Born-Effective Charges in $AgNb_{1/2}Ta_{1/2}O_3$: A Density-Functional and Raman Scattering Study. *J. Am. Ceram. Soc.* **2016**, *99*, 332–339. [CrossRef]
49. Zou, W.N.; Tang, C.X.; Pan, E. Symmetry types of the piezoelectric tensor and their identification. *Proc. R. Soc. A Math. Phys. Eng. Sci.* **2013**, *469*, 20120755. [CrossRef]
50. Kuwata, J.; Uchino, K.; Nomura, S. Electrostrictive coefficients of pb($Mg_{1/3}Nb_{2/3}$)O_3 ceramics. *Jpn. J. Appl. Phys.* **1980**, *19*, 2099–2103. [CrossRef]
51. Khanbabaee, B.; Mehner, E.; Richter, C.; Hanzig, J.; Zschornak, M.; Pietsch, U.; Stöcker, H.; Leisegang, T.; Meyer, D.C.; Gorfman, S. Large piezoelectricity in electric-field modified single crystals of $SrTiO_3$. *Appl. Phys. Lett.* **2016**, *109*, 222901. [CrossRef]
52. Park, D.; Hadad, M.; Riemer, L.M.; Ignatans, R.; Spirito, D.; Esposito, V.; Tileli, V.; Gauquelin, N.; Chezganov, D.; Jannis, D.; et al. Induced giant piezoelectricity in centrosymmetric oxides. *Science* **2022**, *375*, 653. [CrossRef]
53. Catti, M.; Noel, Y.; Dovesi, R. Full piezoelectric tensors of wurtzite and zinc blende ZnO and ZnS by first-principles calculations. *J. Phys. Chem. Solids* **2003**, *64*, 2183–2190. [CrossRef]
54. Kyung, W.; Kim, C.H.; Kim, Y.K.; Kim, B.; Kim, C.; Jung, W.; Kwon, J.; Kim, M.; Bostwick, A.; Denlinger, J.D.; et al. Electric-field-driven octahedral rotation in perovskite. *npj Quantum Mater.* **2021**, *6*, 5. [CrossRef]